ACS OMEGA

Open Access

http://pubs.acs.org/journal/acsodf

Article

$NH_2(CH_3)_2CuCl_3$ Organic–Inorganic Hybrid Perovskite: Consideration to Crystal Structure, Thermodynamics, and Structural Molecular Dynamics

Ae Ran Lim* and Tae Ho Yeom

Cite This: *ACS Omega* 2024, 9, 34918–34926

Read Online

ACCESS | Metrics & More | Article Recommendations

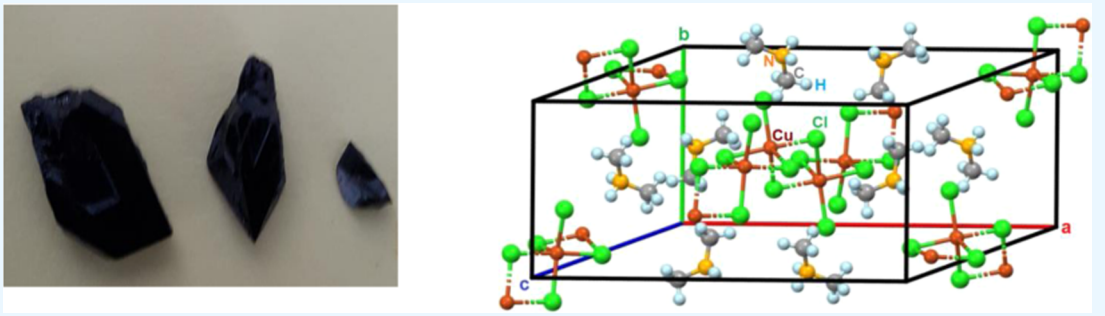

ABSTRACT: The crystal structure of $NH_2(CH_3)_2CuCl_3$, an organic–inorganic hybrid perovskite, undergoes a phase transition from triclinic to monoclinic at the phase transition temperature T_C of 287 K. We investigated the temperature dependencies of NMR chemical shifts and spin–lattice relaxation time $T_{1\rho}$ to gain insights into the structural geometry and molecular dynamics during the transition from phase II to phase I at high temperatures. Analysis of the ^1H and ^{13}C NMR chemical shifts of the cation revealed a continuous change in the surrounding structural geometry with temperature, without any anomalous changes around T_C. The sudden decrease in $T_{1\rho}$ values from low to high temperatures indicated a significant variation in proton and carbon dynamics at T_C, arising from the slowing motion of molecular dynamics across the phase transition. The activation energies E_a obtained from the temperature dependence of $T_{1\rho}$ for ^1H and ^{13}C were larger in phase I than in phase II. This suggests that molecular motions in phase II exhibit a higher degree of freedom compared to those in phase I, where they are more constrained. These findings on $NH_2(CH_3)_2CuCl_3$ are presented to enhance its potential applications by elucidating the crystal configuration and structural molecular dynamics of ABX_3 type compound.

1. INTRODUCTION

The exploration of new materials with exceptional electronic, dielectric, and optical properties holds significant promise for various applications in the development of electronic devices.[1,2] Organic–inorganic hybrid perovskites have garnered considerable attention in optoelectronic devices, such as light-emitting diodes, detectors, photodetectors, and solar cells, owing to their remarkable properties.[3−10] In the field of hybrid halide perovskite materials, research on phase transitions under pressure and the incorporation of copper halides has also garnered significant interest.[11,12] Recently, there has been a growing development in harnessing organic–inorganic hybrid perovskite within field-effect transistor devices, thanks to their multifaceted capabilities.[13,14] The studies as dielectric gates in flexible thin-film transistors, capitalizing on their high permittivity particularly suitable, have been reported.[2,15−17] Among these, ABX_3 perovskites constitute an intriguing class of compounds that exhibit phase transitions alongside changes in their physical and chemical properties. Numerous studies on organic–inorganic hybrid ABX_3 compounds have yielded valuable insights due to their broad applicability. Notably, recent efforts have been focused on the development of materials with ABX_3 stoichiometry, wherein *A* represents a large organic cation (A = $NH_3CH_3^+$, $NH_2(CH_3)^{2+}$, $NH(CH_3)^{3+}$), B denotes a small metal cation (B = Co, Zn, Cu, Mn, Cd), and X stands for a halide anion (X = Cl, Br, I), for highly efficient photovoltaic applications at a reduced cost.[18−24] $NH_2(CH_3)_2CuCl_3$ stands out as an organic-metallic magnetic material exhibiting quasi-one-dimensional alternating ferromagnetic and antiferromagnetic Heisenberg chains, attracting considerable research attention in the past.[25−30]

Received: May 14, 2024
Revised: June 22, 2024
Accepted: July 16, 2024
Published: July 29, 2024

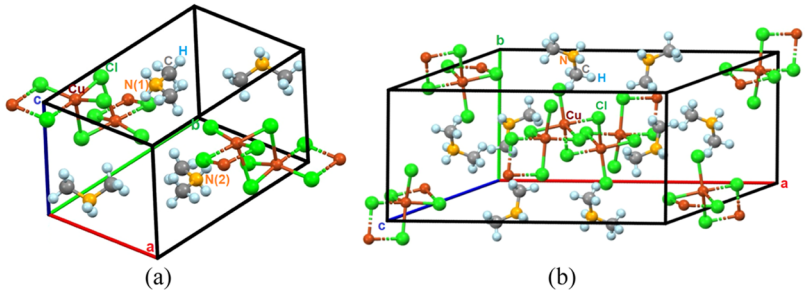

Figure 1. (a) Triclinic structure of $NH_2(CH_3)_2CuCl_3$ crystal at 250 K and (b) monoclinic structure of $NH_2(CH_3)_2CuCl_3$ crystal at 300 K (CCDC 2333813 and 2333814).

Table 1. Crystal Data and Structure Refinement for $NH_2(CH_3)_2CuCl_3$ at 250, 300, and 350 K

temperature	250 K	300 K	350 K
chemical formula	$C_4H_{16}N_2Cu_2Cl_6$	$C_2H_8NCuCl_3$	$C_2H_8NCuCl_3$
weight	431.97	215.98	215.98
crystal system	triclinic	monoclinic	monoclinic
space group	*P*1(bar)	*C*2/*c*	*C*2/*c*
a (Å)	8.659 (4)	17.4774 (9)	17.5129 (10)
b (Å)	9.710 (5)	8.6350 (4)	8.6602 (5)
c (Å)	10.722 (6)	11.9919 (11)	12.0155 (7)
α (deg)	72.396 (17)	90	90
β (deg)	67.506 (16)	125.3550 (10)	125.151 (2)
γ (deg)	64.042 (16)	90	90
Z	2	8	8
V (Å^3)	738.9 (7)	1476.03 (17)	1490.01 (15)
radiation type	Mo−K*α*	Mo−K*α*	Mo−K*α*
wavelength (Å)	0.71073	0.71073	0.71073
reflections collected	13818	15484	13997
independent reflections	3712 (R_{int} = 0.1118)	1833 (R_{int} = 0.0571)	1863 (R_{int} = 0.0577)
goodness-of-fit on F^2	1.005	1.023	1.035
final *R* indices [I > 2sigma(I)]	R_1 = 0.0956, wR_2 = 0.2436	R_1 = 0.0364, wR_2 = 0.0760	R_1 = 0.0377, wR_2 = 0.0777
R indices (all data)	R_1 = 0.1593, wR_2 = 0.2917	R_1 = 0.0682, wR_2 = 0.0907	R_1 = 0.0784, wR_2 = 0.0952

This compound, belonging to the class of organic−inorganic hybrids, has been regarded as an ideal model for ferromagnetic-antiferromagnetic chains.

Previously reported findings indicated that the phase transition, based on the temperature-dependent dielectric constant, occurred at T_C (H) = 282.5 K upon heating and T_C (C) = 245 K upon cooling.[16] Subsequent differential scanning calorimetry (DSC) results, as reported by Park et al.,[31] defined the phase transition temperatures as T_C (H) = 288 K upon heating and T_C (C) = 285 K upon cooling. X-ray experiments[26] further confirmed a structural phase transition from the triclinic to the monoclinic phase near T_C. Additionally, optimization of growth conditions for single crystals of $NH_2(CH_3)_2CuCl_3$ through solvent evaporation methods, utilizing mixed solvents of methanol and isopropanol at varying solution temperatures in a supersaturated solution, has been discussed.[32,33] These studies revealed that the best growth conditions were achieved with a 2:1 (methanol/isopropanol) ratio at 35 °C.

At 300 K, the $NH_2(CH_3)_2CuCl_3$ crystal exhibits a monoclinic space group of *C*12/*c*1, with lattice constants: *a* = 17.416 Å, *b* = 8.5871 Å, *c* = 11.976 Å, *β* = 125.06°, and Z = 4. Conversely, at 175 K, it adopts a triclinic space group of *P*1(bar) with lattice constants: *a* = 8.5522 Å, *b* = 9.6140 Å, *c* = 10.5676 Å, *α* = 73.089°, *β* = 68.389°, *γ* = 64.459°, and *Z* = 2.[21,31,33,34] At 300 K, bibridged $Cu_2Cl_6^{2-}$ dimers are interconnected to form infinite chains with Cu−Cl···Cl−Cu contacts along the *a*-axis. These Cu-halide planes are separated by methyl groups along the *b*-axis. $NH_2(CH_3)_2$ molecules are positioned between these $Cu_2Cl_6^{2-}$ dimer chains, with two parallel chains connected via N−H···Cl hydrogen bonds.[35] The Cu ions are coordinated by 5Cl^- ions, and the coordination numbers of the Cl^- ions surrounding the Cu ions remain unchanged at low temperatures.

This study focuses on $NH_2(CH_3)_2CuCl_3$ single crystals grown via the aqueous solution method, delving into their structure, phase transition temperature, and thermal properties. Moreover, to elucidate structural changes and phase transitions, nuclear magnetic resonance (NMR) chemical shifts for ^{1}H and ^{13}C atoms within the cations of this crystal were analyzed across the temperature range of 180−420 K. Additionally, the energy transfer around ^{1}H and ^{13}C atoms, considering the temperature dependence of the spin−lattice relaxation times $T_{1\rho}$, was investigated. The activation energies (E_a) governing dynamical motion near the phase transition temperature (T_C) were determined. These findings provide crucial insights into the crystal configuration and energy transfer mechanisms for ABX_3-type compounds, offering valuable information for potential applications.

2. RESULTS AND DISCUSSION

2.1. Single Crystal XRD. The single-crystal X-ray diffraction (SCXRD) experimental results for $NH_2(CH_3)_2CuCl_3$ crystals were obtained at temperatures of

https://doi.org/10.1021/acsomega.4c04606
ACS Omega 2024, 9, 34918−34926

Table 2. Bond-lengths (Å) and Bond-angles (deg) for $NH_2(CH_3)_2CuCl_3$ at 250 K

Cu(1)−Cl(3)	2.247(3)	Cl(3)−Cu(1)−Cl(2)	92.69(10)	C(4)−N(2)−H(2AN)	107.9
Cu(1)−Cl(2)	2.290(3)	Cl(3)−Cu(1)−Cl(1)	158.93(12)	C(3)−N(2)−H(2BN)	107.9
Cu(1)−Cl(1)	2.308(3)	Cl(2)−Cu(1)−Cl(1)	92.52(9)	C(4)−N(2)−H(2BN)	107.9
Cu(1)−Cl(1)#1	2.332(3)	Cl(3)−Cu(1)−Cl(1)#1	89.93(10)	H(2AN)-N(2)-H(2BN)	107.2
Cu(2)−Cl(4)	2.272(3)	Cl(2)−Cu(1)−Cl(1)#1	176.60(10)	N(1)−C(1)−H(1A)	109.5
Cu(2)−Cl(5)	2.306(3)	Cl(1)−Cu(1)−Cl(1)#1	84.26(9)	N(1)−C(1)−H(1B)	109.5
Cu(2)−Cl(6)	2.316(3)	Cl(4)−Cu(2)−Cl(5)	92.26(10)	H(1A)-C(1)-H(1B)	109.5
Cu(2)−Cl(6)#2	2.337(3)	Cl(4)−Cu(2)−Cl(6)	154.83(12)	N(1)−C(1)−H(1C)	109.5
Cu(2)−Cl(2)	2.639(3)	Cl(5)−Cu(2)−Cl(6)	92.06(10)	H(1A)-C(1)-H(1C)	109.5
N(1)−C(1)	1.464(13)	Cl(4)−Cu(2)−Cl(6)#2	89.77(10)	H(1B)-C(1)-H(1C)	109.5
N(1)−C(2)	1.475(14)	Cl(5)−Cu(2)−Cl(6)#2	175.40(10)	N(1)−C(2)−H(2A)	109.5
N(1)−H(1AN)	0.9000	Cl(6)−Cu(2)−Cl(6)#2	84.38(9)	N(1)−C(2)−H(2B)	109.5
N(1)−H(1BN)	0.9000	Cl(4)−Cu(2)−Cl(2)	108.51(10)	H(2A)-C(2)-H(2B)	109.5
N(2)−C(3)	1.440(16)	Cl(5)−Cu(2)−Cl(2)	89.88(9)	N(1)−C(2)−H(2C)	109.5
N(2)−C(4)	1.457(13)	Cl(6)−Cu(2)−Cl(2)	96.28(10)	H(2A)-C(2)-H(2C)	109.5
N(2)-H(2AN)	0.9000	Cl(6)#2-Cu(2)−Cl(2)	93.40(9)	H(2B)-C(2)-H(2C)	109.5
N(2)-H(2BN)	0.9000	Cu(1)−Cl(1)−Cu(1)#1	95.74(9)	N(2)−C(3)−H(3A)	109.5
C(1)-H(1A)	0.9700	Cu(1)−Cl(2)−Cu(2)	92.08(9)	N(2)−C(3)−H(3B)	109.5
C(1)-H(1B)	0.9700	Cu(2)−Cl(6)−Cu(2)#2	95.62(9)	H(3A)-C(3)-H(3B)	109.5
C(1)-H(1C)	0.9700	C(1)−N(1)−C(2)	114.2(10)	N(2)−C(3)−H(3C)	109.5
C(2)-H(2A)	0.9700	C(1)−N(1)−H(1AN)	108.7	H(3A)-C(3)-H(3C)	109.5
C(2)-H(2B)	0.9700	C(2)−N(1)−H(1AN)	108.7	H(3B)-C(3)-H(3C)	109.5
C(2)-H(2C)	0.9700	C(1)−N(1)−H(1BN)	108.7	N(2)−C(4)−H(4A)	109.5
C(3)-H(3A)	0.9700	C(2)−N(1)−H(1BN)	108.7	N(2)−C(4)−H(4B)	109.5
C(3)-H(3B)	0.9700	H(1AN)−N(1)-H(1BN)	107.6	H(4A)-C(4)-H(4B)	109.5
C(3)-H(3C)	0.9700	C(3)−N(2)−C(4)	117.8(10)	N(2)−C(4)−H(4C)	109.5
C(4)-H(4A)	0.9700	C(3)−N(2)−H(2AN)	107.9	H(4A)-C(4)-H(4C)	109.5
C(4)-H(4B)	0.9700			H(4B)-C(4)-H(4C)	109.5
C(4)-H(4C)	0.9700				

Table 3. Bond-lengths (Å) and Bond-angles (deg) for $NH_2(CH_3)_2CuCl_3$ at 300 K

Cu(1)−Cl(3)	2.2561(11)	Cl(3)−Cu(1)−Cl(2)	92.29(4)	C(1)−N(1)−H(1BN)	107.1
Cu(1)−Cl(2)	2.2777(10)	Cl(3)−Cu(1)−Cl(1)	155.48(5)	C(2)−N(1)−H(1BN)	107.1
Cu(1)−Cl(1)	2.3078(11)	Cl(2)−Cu(1)−Cl(1)	92.35(4)	H(1AN)-N(1)-H(1BN)	106.8
Cu(1)−Cl(1)#1	2.3189(10)	Cl(3)−Cu(1)−Cl(1)#1	90.00(4)	N(1)−C(1)−H(1A)	109.5
Cu(1)−Cl(2)#2	2.7112(12)	Cl(2)−Cu(1)−Cl(1)#1	176.44(4)	N(1)−C(1)−H(1B)	109.5
N(1)−C(1)	1.417(6)	Cl(1)−Cu(1)−Cl(1)#1	84.44(4)	H(1A)-C(1)-H(1B)	109.5
N(1)−C(2)	1.418(6)	Cl(3)−Cu(1)−Cl(2)#2	106.81(5)	N(1)−C(1)−H(1C)	109.5
N(1)-H(1AN)	0.8900	Cl(2)−Cu(1)−Cl(2)#2	88.56(4)	H(1A)-C(1)-H(1C)	109.5
N(1)-H(1BN)	0.8900	Cl(1)−Cu(1)−Cl(2)#2	97.36(4)	H(1B)-C(1)-H(1C)	109.5
C(1)-H(1A)	0.9600	Cl(1)#1-Cu(1)−Cl(2)#2	93.39(4)	N(1)−C(2)−H(2A)	109.5
C(1)-H(1B)	0.9600	Cu(1)−Cl(1)−Cu(1)#1	95.56(4)	N(1)−C(2)−H(2B)	109.5
C(1)-H(1C)	0.9600	Cu(1)−Cl(2)−Cu(1)#2	89.72(4)	H(2A)-C(2)-H(2B)	109.5
C(2)-H(2A)	0.9600	C(1)−N(1)−C(2)	120.8(4)	N(1)−C(2)−H(2C)	109.5
C(2)-H(2B)	0.9600	C(1)−N(1)−H(1AN)	107.1	H(2A)-C(2)-H(2C)	109.5
C(2)-H(2C)	0.9600	C(2)−N(1)−H(1AN)	107.1	H(2B)-C(2)-H(2C)	109.5

250, 300, and 350 K. At 250 K, the crystal exhibited a triclinic structure with the $P1(\text{bar})$ space group, characterized by lattice parameters: a = 8.659 Å, b = 9.710 Å, c = 10.722 Å, α = 72.396°, β = 67.506°, γ = 64.042°, and Z = 2. Conversely, at 300 K, the crystal structure transitioned to a monoclinic phase with the $C2/c$ space group, featuring lattice constants: a = 17.4774 Å, b = 8.6350 Å, c = 11.9919 Å, and β = 125.3550°, with Z = 8. Notably, the lattice constants at 350 K were found to be almost identical to those observed at 300 K. The structural data indicate a higher symmetry transition from triclinic to monoclinic. Figure 1a,b illustrate the thermal ellipsoids and atomic numbering for each atom within the triclinic structure at 250 K and the monoclinic structure at 300 K, respectively. The crystal structure comprises an organic $NH_2(CH_3)_2$ cation and an inorganic Cu_2Cl_6 anion. Infinite chains are formed by face-shared Cu_2Cl_6 octahedra, with five doubly bridging Cl^- ions linking adjacent Cu centers. The phase transition induces significant changes in the structure, particularly evident in the mode of N−H···Cl hydrogen bonding between $NH_2(CH_3)_2$ cations and Cu_2Cl_6 chains. Detailed SCXRD data collection and refinement information at 250, 300, and 350 K are provided in Table 1. The bond-lengths and bond-angles at 250 K, which shows a triclinic structure, and 300 K, which shows a monoclinic structure, are shown in Tables 2 and 3. Although the N−C, N−H, and C−H bond-lengths in the cations shown in Tables 2 and 3 became shorter at 300 K compared to 250 K, the Cu−Cl bond-lengths were seen to be significantly longer at 300 K compared to 250 K.

https://doi.org/10.1021/acsomega.4c04606
ACS Omega 2024, 9, 34918−34926

This is consistent with the fact that the *a*-axis of the lattice constant becomes longer due to Cu−Cl bond-lengths when the structure changes from triclinic to monoclinic. At 250 K, two symmetry-independent N(1) and N(2) sites exist, whereas only one N site is present at 300 K. This means that the symmetry of the single crystal improves at 300 K. Crystallographic data for temperatures of 250, 300, and 350 K, in the form of CIF files, have been deposited in the Cambridge Data Base (CCDC 2333812−2333814).

2.2. Phase Transition Temperature. DSC analysis of $NH_2(CH_3)_2CuCl_3$ crystals was conducted at a heating and cooling rate of 10 °C/min, using a sample amount of 4.9 mg. The DSC experiment was performed below the decomposition temperature determined by the thermogravimetric analysis (TGA) curve. The resulting DSC curves exhibited a very weak endothermic peak near 287 K upon heating and an exothermic peak near 281 K upon cooling, as depicted in Figure 2. The

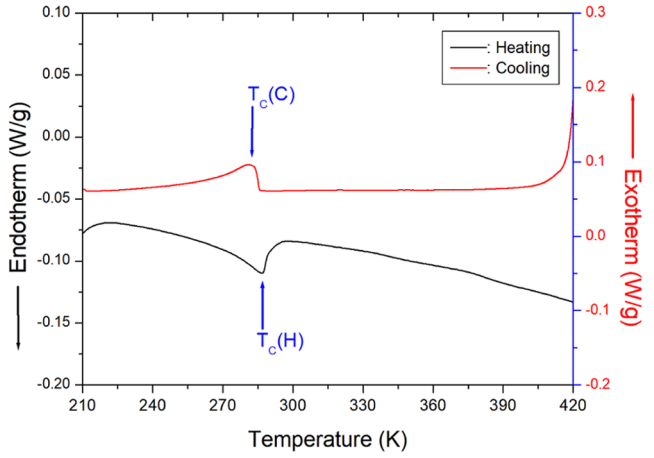

Figure 2. Differential scanning calorimetry curves of $NH_2(CH_3)_2CuCl_3$ at a heating and cooling rate of 10 °C/min.

corresponding enthalpy values for these peaks were measured as 188 J/mol and 707 J/mol, respectively, indicating a thermal hysteresis of ΔT = 6 K. The endothermic peak observed at 287 K signifies the phase transition temperature, marking the transition from a triclinic to monoclinic structure. Variable-temperature optical polarizing microscopy analysis of the morphology revealed that the single crystals remained unchanged until the temperature was increased from 300 to 430 K.

PXRD patterns were obtained above the phase transition temperature using powder samples prepared by grinding single crystals, within the 2θ range of 8−50° (Figure 3a). The PXRD patterns observed at 300 K (black), 350 K (red), and 400 K (blue) were identical. However, patterns obtained above 450 K exhibited a distinct difference from those observed at temperatures below 400 K, and no crystallinity was observed, indicating the onset of melting. Furthermore, simulated XRD patterns based on CIF files at 250, 300, and 350 K are depicted in Figure 3b, demonstrating good agreement with the experimental patterns shown in Figure 3a. This observation correlates well with the endothermic peak detected at 287 K in the DSC results, suggesting that this peak is associated with the phase transition temperature, T_C (= 287 K). The data are consistent with highering of the symmetry from a triclinic space group *P*1(bar) to the monoclinic space group *C*2/*c*. Moreover, the peaks identified in this diffractogram were

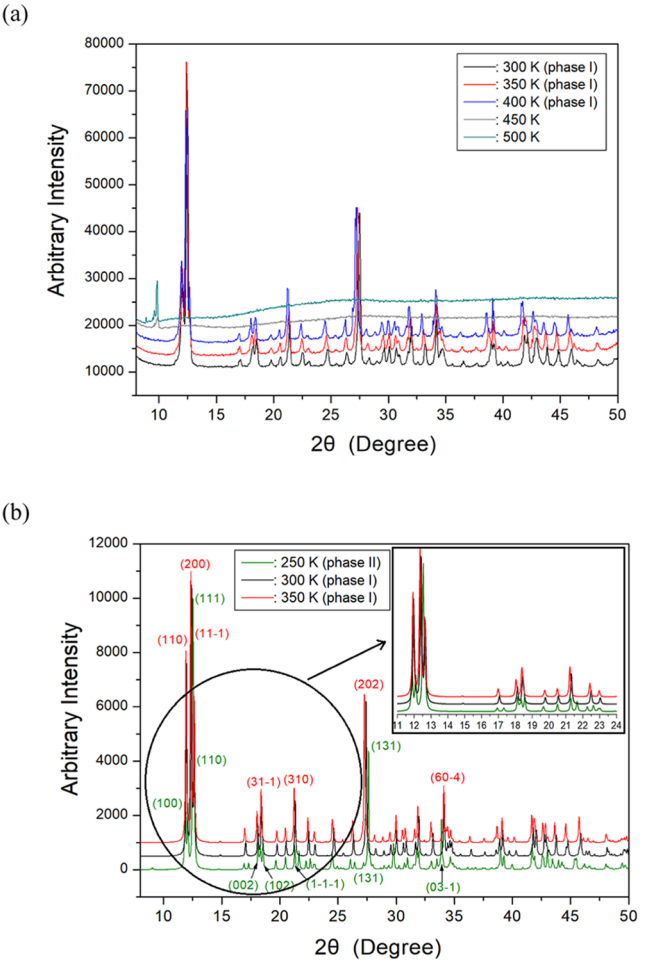

Figure 3. (a) The powder X-ray diffraction patterns of $NH_2(CH_3)_2CuCl_3$ at 300, 350, 400, 450, and 500 K and (b) The simulation X-ray diffraction patterns obtained by single-crystal X-ray diffraction of $NH_2(CH_3)_2CuCl_3$ at 250, 300, and 350 K.

indexed using the Mercury program.[36,37] Notably, the very strong peak observed at approximately 12.4° of 2θ in both the PXRD and simulated pattern at 300 K corresponds to the (200) reflection, while the strong peak at approximately 12.54° in the simulated pattern at 250 K corresponds to the (110) reflection, as illustrated and enlarged in Figure 3b.

2.3. Thermodynamic Property. To comprehend the thermodynamic stability of $NH_2(CH_3)_2CuCl_3$, simultaneous TGA and DTA thermal analyses were conducted within the temperature range of 300 to 900 K, with increasing temperature as illustrated in Figure 4. The TGA experiment utilized a sample amount of 7.56 mg and employed the same heating rate of 10 °C/min as measured by DSC. In the TGA curve, the partial decomposition temperature (T_d), indicative of a 2% weight loss, was determined to be approximately 481 K, signifying the thermal stability of the material up to this temperature. As the temperature increased, the weight loss of $NH_2(CH_3)_2CuCl_3$ crystals exhibited a rapid decline. The DTA curve depicted an endothermic peak near 458 K, which aligned well with the melting temperature observed through the morphology of single crystals using a polarizing microscope equipped with a hot stage. Additionally, a prominent peak observed at 562 K indicated a 38% reduction in molecular weight, calculated from the total molecular weight, attributed to the partial decomposition of $NH_2(CH_3)_2Cl$. Approximately

https://doi.org/10.1021/acsomega.4c04606
ACS Omega 2024, 9, 34918−34926

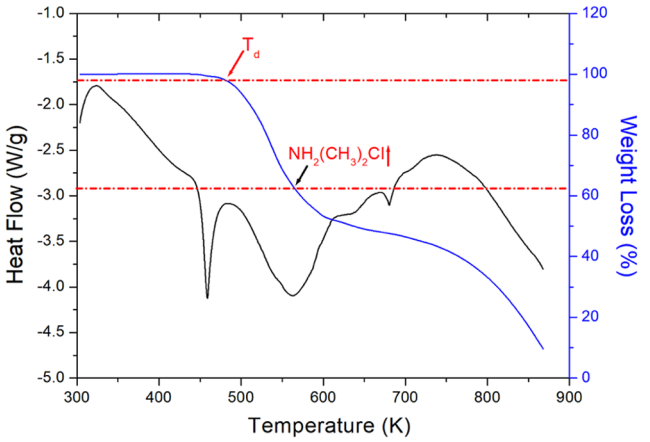

Figure 4. Thermal properties of $NH_2(CH_3)_2CuCl_3$: the thermogravimetry analysis and differential thermal analysis curves of $NH_2(CH_3)_2CuCl_3$.

60% of the total weight loss occurred within the range of 500−650 K, with complete weight loss observed around 900 K.

2.4. ^{1}H and ^{13}C MAS NMR Chemical Shifts. Structural analysis was conducted by monitoring ^{1}H in $NH_2(CH_3)_2CuCl_3$ using MAS NMR at increasing temperatures. The ^{1}H NMR spectra for NH_2 and CH_3 at 300 K, shown inset of Figure 5,

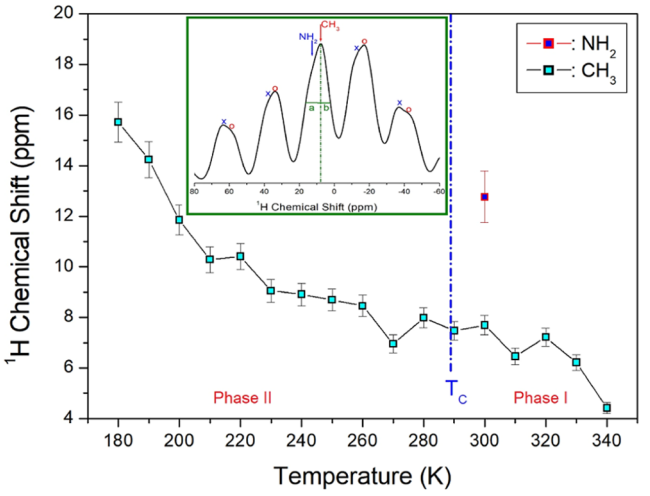

Figure 5. ^{1}H NMR chemical shifts of $NH_2(CH_3)_2CuCl_3$ with increasing temperature (Inset: The ^{1}H NMR spectrum at 300 K, and the crosses and open circles are sidebands for NH_2 and CH_3, respectively).

revealed that the line widths represented by symbols 'a' and 'b' at the full-width at half-maximum (fwhm) value were not identical. This asymmetry in the signal is attributed to the overlapping lines of the two ^{1}H nuclei for NH_2 and CH_3 within the $NH_2(CH_3)_2$ cations, with their overlapping sidebands for the ^{1}H spectrum represented as crosses and open circles, respectively. The ^{1}H chemical shift for NH_2, which can be distinguished into sidebands, was recorded at approximately 12.77 ppm, while the ^{1}H chemical shift for CH_3 was obtained at approximately 7.71 ppm. Moreover, the NMR chemical shifts for ^{1}H were recorded at phases II and I, as depicted in Figure 5. The ^{1}H NMR chemical shifts decreased continuously with increasing temperature, without exhibiting any anomalous changes near T_C. This continuous change in NMR chemical shifts, attributable to variations in the local field around the ^{1}H nuclei, indicates alterations in the crystallographic geometry, without any anomalous changes near T_C.

The temperature dependencies of the ^{13}C NMR chemical shifts for $NH_2(CH_3)_2CuCl_3$ are depicted in Figure 6. The ^{13}C

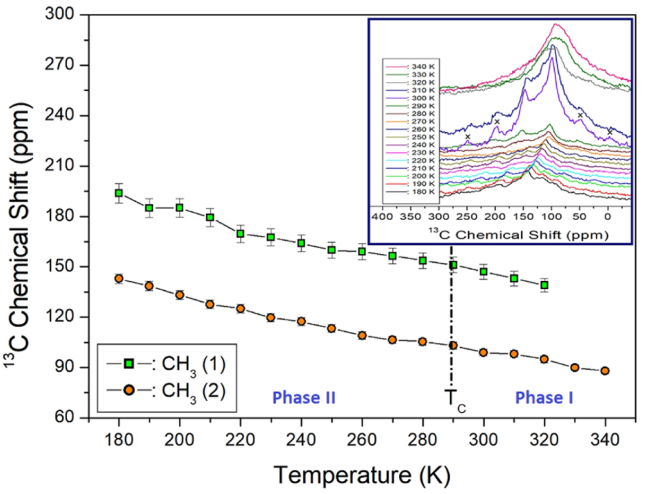

Figure 6. ^{13}C NMR chemical shifts of $NH_2(CH_3)_2CuCl_3$ with increasing temperature (Inset: Temperature-dependence of ^{13}C NMR spectrum).

MAS NMR spectrum at 300 K exhibited two resonance signals, as shown in the inset of Figure 6, with ^{13}C chemical shifts recorded at 147.02 and 98.89 ppm, corresponding to $CH_3(1)$ and $CH_3(2)$, respectively. With increasing temperature, the NMR chemical shifts for $CH_3(1)$ and $CH_3(2)$ displayed almost identical trends, gradually shifting toward lower values without exhibiting any anomalous changes near T_C. This continuous change in the NMR chemical shifts, attributed to variations in the local field around the ^{13}C nuclei, suggests alterations in the crystallographic geometry. The trend observed in the ^{13}C chemical shifts mirrored the change observed in ^{1}H, indicating that the sources of interactions between the atoms and ions surrounding the ^{1}H and ^{13}C nuclei are similar.

Organic molecules exhibit a temperature-dependent chemical shift, especially when in proximity to heavy metals like Cd.[38] However, the chemical shift of $NH_2(CH_3)_2CuCl_3$ was not significantly affected by temperature.

2.5. NMR Spin−lattice Relaxation Times for ^{1}H and ^{13}C. The changes in the intensity of the ^{1}H and ^{13}C NMR signals were recorded at a specific temperature, varying the delay times. The relationship with the decay rate of the magnetization was defined by the spin−lattice relaxation time, $T_{1\rho}$[39−41]

$$P(\tau) = A\exp(-\tau/T_{1\rho}) \quad (1)$$

In the eq 1, $P(\tau)$ represents the signal intensities at each delay time τ. One of them, the signals of the ^{13}C NMR for delay times in the range of 0.1−10 ms at 300 K are shown in Figure 7. The ^{1}H $T_{1\rho}$ and ^{13}C $T_{1\rho}$ values for $NH_2(CH_3)_2CuCl_3$ were derived from the slope of the intensity vs delay time plot using eq 1. As depicted in Figure 8, the ^{1}H $T_{1\rho}$ and ^{13}C $T_{1\rho}$ values were on the order of milliseconds, with the ^{13}C $T_{1\rho}$ values approximately 10 times longer than the ^{1}H $T_{1\rho}$ values. Below T_C, both the ^{1}H and ^{13}C $T_{1\rho}$ values exhibited a gradual

https://doi.org/10.1021/acsomega.4c04606
ACS Omega 2024, 9, 34918−34926

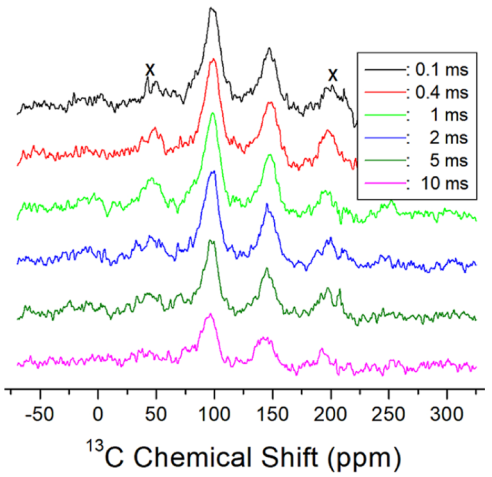

Figure 7. ^{13}C recovery traces by the delay times between 0.1−10 ms at 300 K.

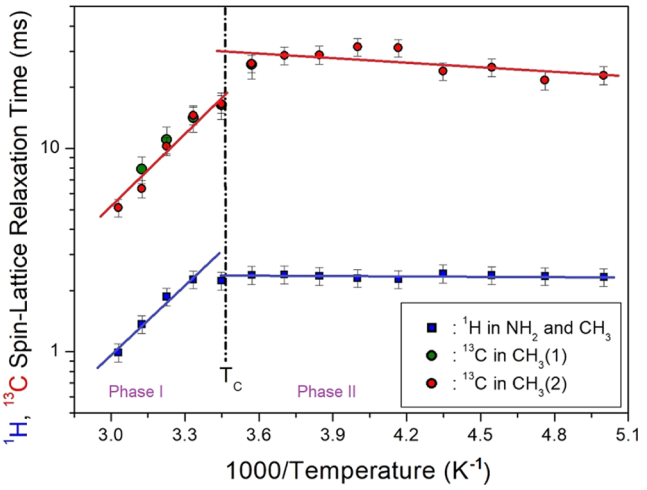

Figure 8. ^{1}H and ^{13}C spin−lattice relaxation times in $NH_2(CH_3)_2CuCl_3$ as a function of inverse temperature. The slopes by solid lines are represented the activation energies.

increase. Conversely, above T_C, the ^{13}C $T_{1\rho}$ values exhibited a rapid decrease. The Arrhenius plots for the $T_{1\rho}$ molecular motions with relaxation time are divided into fast- and slow-motion regions. Fast motion is represented as $\omega_1\tau_C \ll 1$, $T_{1\rho}^{-1} \propto \exp(E_a/k_BT)$ and the slow motion as $\omega_1\tau_C \gg 1$, $T_{1\rho}^{-1} \propto \omega_1^{-2}\exp(-E_a/k_BT)$.[41] The plot is separated into different motion regions at T_C. The ^{1}H $T_{1\rho}$ and ^{13}C $T_{1\rho}$ values at low temperatures resided in the fast-motion region, while the ^{13}C $T_{1\rho}$ and ^{1}H $T_{1\rho}$ values at high temperatures were attributed to the slow-motion region.

Based on Bloembergen-Purcell-Pound (BPP) theory, the experimental values of $T_{1\rho}$ can be expressed by the correlation time τ_C for reorientational motion, and $T_{1\rho}$ for molecular motion as follows[39,42,43]

$$\begin{aligned} 1/T_{1\rho} = R\{&4\tau_C/[1+\omega_1^2\tau_C^2] + \tau_C/[1+(\omega_C-\omega_H)^2\tau_C^2] \\ &+ 3\tau_C/[1+\omega_C^2\tau_C^2] \\ &+ 6\tau_C/[1+(\omega_C+\omega_H)^2\tau_C^2] \\ &+ 6\tau_C/[1+\omega_H^2\tau_C^2]\} \\ = A\exp(&-E_a/k_BT) \end{aligned} \quad (2)$$

where R is a constant, ω_1 is the spin-locking field, and ω_C and ω_H are the Larmor frequencies of ^{13}C and ^{1}H, respectively. Local field fluctuations are induced by thermal motion, activated by thermal energy. The ^{1}H and ^{13}C $T_{1\rho}$ values exhibited similar variations due to similar molecular motions of the C−H bond. $T_{1\rho}$ is generally expressed by an Arrhenius-type equation based on the activation energy E_a for molecular motion and temperature. The E_a for ^{1}H, obtained from the slope of the $T_{1\rho}$ vs 1000/temperature plot represented by blue squares in Figure 8 at low and high temperatures, was 0.06 ± 0.02 and 22.29 ± 3.63 kJ/mol, respectively. Additionally, the E_a for ^{13}C, obtained from the slope of $T_{1\rho}$ vs 1000/temperature represented by red circles in Figure 8 at low and high temperatures, was 0.08 ± 0.01 and 21.41 ± 2.49 kJ/mol, respectively.

3. CONCLUSIONS

The data confirm that the $NH_2(CH_3)_2CuCl_3$ crystal undergoes a transformation from a triclinic to monoclinic structure at a phase transition temperature of 287 K. The thermal stability of the crystal was determined to be 481 K by TGA results. The temperature dependence of NMR chemical shifts and $T_{1\rho}$ for the perovskite-type $NH_2(CH_3)_2CuCl_3$ crystal were investigated to understand the structural geometry and changes in molecular dynamics during the high-temperature transition from phase II to phase I. Analysis of the ^{1}H and ^{13}C NMR chemical shifts of the cation with temperature revealed that the surrounding structural geometry underwent a continuous change, without any anomalous changes around T_C. This suggests that the crystallographic geometry evolves smoothly through the phase transition, contributing to a comprehensive understanding of the material's behavior.

The sudden drop in $T_{1\rho}$ values from low temperature up to high temperature indicates a sudden variation in the proton and carbon dynamics at T_C, stemming from the slowing motion of molecular dynamics across the phase transition. These abrupt changes in $T_{1\rho}$ near T_C suggest a sudden variation in the energy transfer in the vicinity of the protons and carbons. Below T_C, both ^{1}H and ^{13}C $T_{1\rho}$ values were in the fast-motion region, whereas above T_C, they shifted to the slow-motion region. This transition reflects a change caused by a structural phase transition. The activation energy (E_a) obtained from the temperature dependence of $T_{1\rho}$ for ^{1}H and ^{13}C exhibited larger values in phase I than in phase II. This suggests that molecular motions in phase II were highly free, whereas in phase I, they lacked a large degree of freedom. The small E_a values for phase II indicate a substantial degree of freedom for the NH_2 and CH_3 groups, respectively. Conversely, in phase I, the large Ea values were primarily attributed to the overall molecular motion of $NH_2(CH_3)_2$ groups. Consequently, the phase transition mechanisms of $NH_2(CH_3)_2CuCl_3$ at high temperature possibly involve the reorientation of the $NH_2(CH_3)_2$ group. The results of this study on organic−inorganic hybrid perovskite-type $NH_2(CH_3)_2CuCl_3$ are expected to facilitate their potential applications in various electrochemical devices such as supercapacitors, batteries, and fuel cells.

4. EXPERIMENTAL SECTION

4.1. Crystal Growth. Single crystals of $NH_2(CH_3)_2CuCl_3$ were cultivated utilizing $NH_2(CH_3)_2Cl$ (Aldrich, 98%) and $CuCl_2$ (Aldrich, 98%) in a 1:1 molecular weight ratio within an

https://doi.org/10.1021/acsomega.4c04606
ACS Omega 2024, 9, 34918−34926

aqueous solution. To initiate crystal growth, $NH_2(CH_3)_2CuCl_3$ crystals were dissolved in distilled water at a slightly elevated temperature to induce supersaturation. Following this, the solution was vigorously stirred for 4 h to ensure homogeneity. The single crystals were then harvested from the uniform solution via slow evaporation maintained at a constant temperature of 303 K. After several weeks, the resulting crystals were observed to be dark brown in color, as shown in Figure 9.

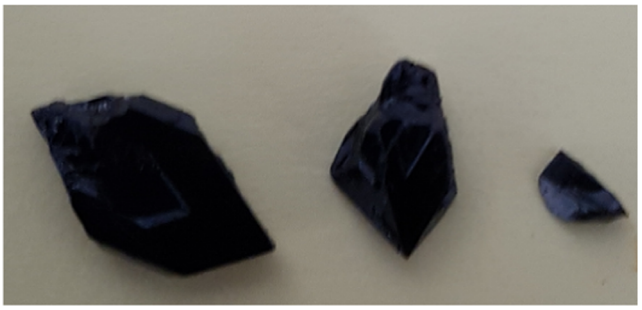

Figure 9. Single crystals grown by the aqueous solution method (the photo was taken by the author A.R. Lim).

4.2. Characterization. The thermal properties of $NH_2(CH_3)_2CuCl_3$ were assessed through a series of experiments, including differential scanning calorimetry (DSC), thermogravimetry analysis (TGA), and differential thermal analysis (DTA) utilizing TA Instruments. These experiments were conducted within the temperature range of 200−900 K under a dry nitrogen gas atmosphere. Additionally, observations regarding the variations in crystal morphology in response to temperature changes were made using an optical polarizing microscope (Carl Zeiss) equipped with a hot stage (Linkam THMS 600).

The crystal structure of $NH_2(CH_3)_2CuCl_3$ at temperatures of 250, 300, and 350 K was determined utilizing both single-crystal X-ray diffraction (SCXRD) and powder X-ray diffraction (PXRD) techniques at the Korea Basic Science Institute (KBSI), Seoul Western Centre. For the SCXRD experiment, a Bruker D8 Venture PHOTON III M14 system equipped with a graphite-monochromated Mo−Kα target and a Cryocool NeverIce low-temperature device was employed. Data collection utilized the SMART APEX3 and SAINT programs, and absorption correction was carried out using the multiscan method in SADABS. The single-crystal structure was analyzed via direct methods and refined using least-squares on F^2 with the SHELXTL program.[39,44] Anisotropic refinement was performed for all non-hydrogen atoms, while hydrogen atoms were included at geometrically ideal positions. In addition, powder X-ray diffraction (PXRD) patterns were obtained at temperatures of 300, 350, 400, 450, and 500 K using an XRD spectrometer featuring a Mo−Kα radiation source.

NMR spectra of $NH_2(CH_3)_2CuCl_3$ crystals were acquired using a solid-state Bruker 400 MHz Avance II+ NMR spectrometer at KBSI. ^{1}H magic angle spinning (MAS) NMR experiments were conducted at the Larmor frequency of $\omega_o/2\pi$ = 400.13 MHz, while ^{13}C MAS NMR experiments were carried out at the Larmor frequency of $\omega_o/2\pi$ = 100.61 MHz, both as a function of temperature. MAS NMR measurements of the samples in cylindrical zirconia rotors of 4 mm were performed at a spinning rate of 5−10 kHz to reduce the spinning sideband, and chemical shifts were referenced to tetramethylsilane (TMS). One-dimensional (1D) NMR spectra for ^{1}H and ^{13}C were obtained with a delay time of 0.1 s. For determining spin−lattice relaxation time values ($T_{1\rho}$) in the rotating system, intensities of ^{1}H and ^{13}C NMR signals were measured with delay times ranging from 10 μs to 20 ms. Data acquisition for ^{1}H and ^{13}C involved a 90° pulse with a delay of 4 μs. Temperature-dependent NMR spectra were collected between 180 and 430 K, with precise temperature control achieved through regulation of N_2 gas flow and heater current, ensuring an accuracy of ±0.5 K.

■ ASSOCIATED CONTENT

Accession Codes

Data sets generated and/oranalyzed during the current study are available in the CCDC 2333812−2333814.

■ AUTHOR INFORMATION

Corresponding Author

Ae Ran Lim − *Graduate School of Carbon Convergence Engineering, Jeonju University, Jeonju 55069, South Korea; Department of Science Education, Jeonju University, Jeonju 55069, South Korea;* orcid.org/0000-0002-5242-9189; Phone: +82-(0)63-220-2514; Email: arlim@jj.ac.kr, aeranlim@hanmail.net

Author

Tae Ho Yeom − *Department of Energy Convergence Engineering, Cheongju University, Cheongju 28503, South Korea*

Complete contact information is available at: https://pubs.acs.org/10.1021/acsomega.4c04606

Notes

The authors declare no competing financial interest.

■ ACKNOWLEDGMENTS

This work was supported by the National Research Foundation of Korea (NRF) grant funded by the Korean Government (MSIT) (2023R1A2C2006333) and the Basic Science Research Program through the NRF, funded by the Ministry of Education, Science, and Technology (2016R1A6A1A03012069).

■ REFERENCES

(1) Senanayak, S. P.; Abdi-Jalebi, M.; Kamboj, V. S.; Carey, R.; Shivanna, R.; Tian, T.; Schweicher, G.; Wang, J.; Giesbrecht, N.; Nuzzo, D. D.; Beere, H. E.; Docampo, P.; Ritchie, D. A.; Fairen-Jimenez, D.; Friend, R. H.; Sirringhaus, H. A general approach for hysteresis-free, operationally stable metal halide perovskite field-effect transistors. *Sci. Adv.* **2020**, *6*, No. eaaz4948.

(2) Kalthoum, R.; Bechir, M. B.; Rhaiem, A. B.; Gargouri, M. $MCdCl_3$ (M = CH_3NH_3, $(CH_3)_2NH_2$): New Hybrid Perovskites with Large Dielectric Constants for Field-Effect Transistors. *Phys. Status Solidi A* **2021**, *218*, No. 2100485.

(3) Ji, C.; Wang, P.; Wu, Z.; Sun, Z.; Li, L.; Zhang, J.; Hu, W.; Hong, M.; Luo, J. Inch-Size Single Crystal of a Lead-Free Organic−Inorganic Hybrid Perovskite for High-Performance Photodetector. *Adv. Funct. Mater.* **2018**, *28*, No. 1705467.

(4) Liao, Q.; Jin, X.; Fu, H. Tunable Halide Perovskites for Miniaturized Solid-State Laser Applications. *Adv. Opt. Mater.* **2019**, *7*, No. 1900099.

(5) Zhang, Q.; Ha, S. T.; Liu, X.; Sum, T. C.; Xiong, Q. Room-Temperature Near-Infrared High-Q Perovskite Whispering-Gallery Planar Nanolasers. *Nano Lett.* **2014**, *14*, 5995−6001.
(6) Geffroy, C.; Grana, E.; Bessho, T.; Almosni, S.; Tang, Z.; Sharma, A.; Kinoshita, T.; Awai, F.; Cloutet, E.; Toupance, T.; Segawa, H.; Hadziioannou, G. p-Doping of a Hole Transport Material via a Poly(ionic liquid) for over 20% Efficiency and Hysteresis-Free Perovskite Solar Cells. *ACS Appl. Energy Mater.* **2020**, *3*, 1393−1401.
(7) Yakunin, S.; Dirin, D. N.; Shynkarenko, Y.; Morad, V.; Cherniukh, I.; Nazarenko, O.; Kreil, D.; Nauser, T.; Kovalenko, M. V. Detection of gamma photons using solution-grown single crystals of hybrid lead halide perovskites. *Nat. Photonics* **2016**, *10*, 585−589.
(8) Bao, C.; Yang, J.; Bai, S.; Xu, W.; Yan, Z.; Xu, Q.; Liu, J.; et al. High Performance and Stable All-Inorganic Metal Halide Perovskite-Based Photodetectors for Optical Communication Applications. *Adv. Mater.* **2018**, *30*, No. 1803422.
(9) Dou, L.; Yang, Y. M.; You, J.; Hong, Z.; Chang, W. H.; Li, G.; Yang, Y. Solution-processed hybrid perovskite photodetectors with high detectivity. *Nat. Commun.* **2014**, *5*, No. 5404.
(10) Bujak, M.; Siodlak, D. Isostructural inorganic-organic piperazine-1,4-diium chloride- and bromidoantimonate (III) monohydrates: octahedral distortions and hydrogen bonds. *Molecules* **2020**, *25*, No. 1361.
(11) Dastidar, R. G.; Okamoto, T.; Takahashi, K.; Takano, Y.; Vijayakumar, C.; Subtahmanyam, C.; Biju, V. Dual-color photoluminescence modulation of zero-dimensional hybrid copper halide microcrystals. *Nanoscale* **2024**, *16*, 5107−5114.
(12) Ghimire, S.; Takahashi, K.; Takano, Y.; Nakamura, T.; Biju, V. Photon recycling by energy transfer in piezochemically synthesized and close-packed methylammonium lead halide perovskites. *J. Phys. Chem. C* **2019**, *123*, 27752−27758.
(13) Daus, A.; Roldán-Carmona, C.; Domanski, K.; Knobelspies, S.; Cantarella, G.; Vogt, C.; Grätzel, M.; Nazeeruddin, M. K.; Tröster, G. Metal-halide perovskites for gate dielectrics in field-effect transistors and photodetectors enabled by PMMA lift-off process. *Adv. Mater.* **2018**, *30*, No. 1707412.
(14) Inagaki, Y.; Sakamoto, Y.; Morodomi, H.; Kawae, T.; Yoshida, Y.; Asano, T.; Hosoi, K.; Kobayashi, H.; Kitagawa, H.; Ajiro, Y.; Furukawa, Y. Unusual magnetic ordering observed in nanosized S = 1/2 quantum spin system $(CH_3)_2NH_2CuCl_3$. *J. Phys. Soc. Jpn.* **2014**, *83*, No. 054716.
(15) Juarez-Perez, E. J.; Sanchez, R. S.; Badia, L.; Garcia-Belmonte, G.; Kang, Y. S.; Mora-Sero, I.; Bisquert, J. Photoinduced Giant Dielectric Constant in Lead Halide Perovskite Solar Cells. *J. Phys. Chem. Lett.* **2014**, *5*, 2390−2394.
(16) Daus, A.; Roldan-carmona, C.; Domanski, K.; Knobelspies, S.; Cantarella, G.; Vogt, C.; Troster, G.; et al. Metal-Halide Perovskites for Gate Dielectrics in Field-Effect Transistors and Photodetectors Enabled by PMMA Lift-Off Process. *Adv. Mater.* **2018**, *30*, No. 1707412.
(17) Wang, Z.-X.; Zhang, H.; Wang, F.; Cheng, H.; He, W.-H.; Liu, Y.-H.; Huang, X.-Q.; Li, P.-F. Superior Transverse Piezoelectricity in a Halide Perovskite Molecular Ferroelectric Thin Film. *J. Am. Chem. Soc.* **2020**, *142*, 12857−12864.
(18) Senanayak, S. P.; Abdi-Jalebi, M.; Kamboj, V. S.; Carey, R.; Shivanna, R.; Tian, T.; Schweicher, G.; et al. A general approach for hysteresis-free, operationally stable metal halide perovskite field-effect transistors. *Sci. Adv.* **2020**, *6*, No. eaaz4948.
(19) Kalthoum, R.; Bechir, M. B.; Rhaiem, A. B.; Dhaou, M. H. Optical properties of new organic-inorganic hybrid perovskites $(CH_3)_2NH_2CdCl_3$ and $CH_3NH_3CdCl_3$ for solar cell applications. *Opt. Mater.* **2022**, *125*, No. 112084.
(20) Jellali, H.; Msalmi, R.; Smaoui, H.; Elleuch, S.; Tozri, A.; Roisnel, T.; Mosconi, E.; Althubiti, N. A.; Naïli, H. Zn^{2+} and Cu^{2+} doping of one-dimensional lead-free hybrid perovskite ABX_3 for white light emission and green solar cell applications. *Mater. Res. Bull.* **2022**, *151*, No. 111819.
(21) Kapustyanyk, V. B.; Korchak, Y. M.; Bazhan, V. V.; Éliyashevskii, Y. I. Temperature Change in the Electronic Spectra of an $NH_2(CH_3)_2CuCl_3$ Crystal in Phase Transitions. *J. Appl. Spectrosc.* **2002**, *69*, 406−412.
(22) Willett, R. D. Crystal Structure and Optical Properties of $(CH_3)_2NH_2CuCl_3$. *J. Chem. Phys.* **1966**, *44*, 39−42.
(23) Hurley, M.; Gerstein, B. C. Low temperature heat capacities of one dimensional systems: Dimethylammonium trichlorocuprate(II) and tetramethylammonium trichloronickelate(II). *J. Chem. Phys.* **1973**, *59*, 6667−6676.
(24) Stone, M. B.; Tian, W.; Granroth, G. E.; Lumsden, M. D.; Chung, J.-H.; Mandrus, D. G.; Nagler, S. E. Spin dynamics of the low-dimensional magnet $(CH_3)_2NH_2CuCl_3$. *Phys. B: Condens. Matter* **2006**, *385*−*386*, 438−440.
(25) Sakamoto, Y.; Morodomi, H.; Inagaki, Y.; Kawae, T.; Asano, T.; Ajiro, Y. Low-Temperature Magnetization Study of Spin Gap System $(CH_3)_2NH_2CuCl_3$ with Nanometer Particle Size. *J. Phys.: Conf. Ser.* **2012**, *400*, No. 032077.
(26) Lahiry, S.; Kakkar, R. On the magnetism of a so-called one-dimensional crystal, dimethylammonium trichlorocuprate(II), DMA-CuCl3. *Chem. Phys. Lett.* **1981**, *78*, 379−382.
(27) Inagaki, Y.; Kobayashi, A.; Asano, T.; Sakon, T.; Kitagawa, H.; Motokawa, M.; Ajiro, Y. Novel Alternating Dimer Chain System $(CH_3)_2NH_2CuCl_3$ Studied by X-ray Structural Analyses and Magnetization Process. *J. Phys. Soc. Jpn.* **2005**, *74*, 2683−2686.
(28) Yoshida, Y.; Wada, O.; Inagaki; Asano, Y. T.; Takeo, K.; Kawae, T.; Takeda, K.; Ajiro, Y. Specific Heat Study of Novel Spin-Gapped System: $(CH_3)_2NH_2CuCl_3$. *J. Phys. Soc. Jpn.* **2005**, *74*, 2917−2920.
(29) Chen, L. M.; Wang, X. M.; Ke, W. P.; Zhao, Z. Y.; Liu, X. G.; Fan, C.; Li, Q. J.; Zhao, X.; Sun, X. F. Heat transport of the quasi-one-dimensional alternating spin chain material $(CH_3)_2NH_2CuCl_3$. *Phys. Rev. B* **2011**, *84*, No. 134429.
(30) Yoshida, M.; Kitano, Y.; Inagaki, Y.; Sakurai, T.; Kimata, M.; Okubo, S.; Ohta, H.; Koyama, K.; Motokawa, M.; Asano, T.; Ajiro, Y. Observation of Direct Transitions in the Ferromagnetic and Antiferromagnetic Dimer System $(CH_3)_2NH_2CuCl_3$ by High-Field ESR. *J. Phys. Soc. Jpn.* **2007**, *76*, No. 113704.
(31) Inagaki, Y.; Sakamoto, Y.; Morodomi, H.; Kawae, T.; Yoshida, Y.; Asano, T.; Hosoi, K.; Kobayashi, H.; Kitagawa, H.; Ajiro, Y.; Furukawa, Y. Unusual Magnetic Ordering Observed in Nanosized S = 1/2 Quantum Spin System $(CH_3)_2NH_2CuCl_3$. *J. Phys. Soc. Jpn.* **2014**, *83*, No. 054716.
(32) Park, G.; Oh, I. W.; Park, J. M. S.; Park, S.-H.; Hong, C. S.; Lee, K.-S. Large-scale single-crystal growth of $(CH_3)_2NH_2CuCl_3$ for neutron scattering experiments. *J. Cryst. Growth* **2016**, *441*, 46−51.
(33) Chen, L. M.; Tao, W.; Zhao, Z. Y.; Li, Q. J.; Ke, W. P.; Wang, X. M.; Liu, X. G.; Fan, C.; Sun, X. F. Growth of $(CH_3)_2NH_2CuCl_3$ single crystals using evaporation method with different temperatures and solvents. *J. Cryst. Growth* **2010**, *312*, 3243−3246.
(34) Willett, R. D.; Twamley, B.; Montfrooij, W.; Granroth, G. E.; Nagler, S. E.; Hall, D. W.; Park, J.-H.; Watson, B. C.; Meisel, M. C.; Talham, D. R. Dimethylammonium Trichlorocuprate (II): Structural Transition, Low-Temperature Crystal Structure, and Unusual Two-Magnetic Chain Structure Dictated by Nonbonding Chloride−Chloride Contacts. *Inorg. Chem.* **2006**, *45*, 7689−7697.
(35) Eckardt, K.; Svoboda, I.; Pabst, I. Crystal structure of dimethylammonium-trichlorocuprate, $(CH_3)_2NH_2(CuCl_3)$. *Z. Kristallogr. - Cryst. Mater.* **1993**, *208*, No. 253.
(36) Mercury 4.0, Program for Crystal Structure Visualisation, Exploration and Data Analysis from the Cambridge Crystallographic Data Center, 2001−2016.
(37) Macrae, C. F.; Sovago, I.; Cottrell, S. J.; Galek, P. T. A.; McCabe, P.; Pidcock, E.; Platings, M.; Shields, G. P.; Stevens, J. S.; Towler, M.; Wood, P. A. *Mercury 4.0*: from visualization to analysis, design and prediction. *J. Appl. Crystallogr.* **2020**, *53*, 226−235.
(38) Biju, V.; Makita, Y.; Sonoda, A.; Yokoyama, H.; Baba, Y.; Ishikawa, M. Temperature-sensitive photoluminescence of CdSe quantum dot clusters. *J. Phys. Chem. B* **2005**, *109*, 13899−13905.
(39) Lim, A. R.; Yoon, M. B. Crystal growth, phase transition, and nuclear magnetic resonance of organic−inorganic hybrid perovskite $NH_2(CH_3)_2CdCl_3$. *RSC Adv.* **2023**, *13*, 26015−26022.

https://doi.org/10.1021/acsomega.4c04606
ACS Omega 2024, 9, 34918−34926

(40) Harris, R. K. *Nuclear Magnetic Resonance Spectroscopy*; Pitman Pub., UK, 1983.
(41) Koenig, J. L. *Spectroscopy of Polymers*; Elsevier, 1999.
(42) Abragam, A. *The Principles of Nuclear Magnetism*; Oxford University Press, 1961.
(43) Bloembergen, N.; Purcell, E. M.; Pound, R. V. Relaxation effects in nuclear magnetic resonance absorption. *Phys. Rev.* **1948**, *73*, No. 679.
(44) Bruker AXS, Inc.. *SHELLXTL*, v6.10; Madison, Wisconsin, USA, 2000.

https://doi.org/10.1021/acsomega.4c04606
ACS Omega 2024, 9, 34918−34926